Research Square

Preprints are preliminary reports that have not undergone peer review.
They should not be considered conclusive, used to inform clinical practice,
or referenced by the media as validated information.

Hydrogen-bond dynamics, proton transfer, and water mobility in crystalline guanidinium carbonates for direct air capture

Xiaoping Wang

wangx@ornl.gov

Oak Ridge National Laboratory https://orcid.org/0000-0001-7143-8112

Sylwia Pawledzio

Oak Ridge National Laboratory

Thiago Pinheiro dos Santos

Oak Ridge National Laboratory

Debmalya Ray

Oak Ridge National Laboratory

Jeffrey Einkauf

Oak Ridge National Laboratory

Radu Custelcean

Oak Ridge National Laboratory https://orcid.org/0000-0002-0727-7972

Vyacheslav Bryantsev

Oak Ridge National Laboratory https://orcid.org/0000-0002-6501-6594

Article

Keywords:

Posted Date: October 29th, 2026

DOI: https://doi.org/10.21203/rs.3.rs-11211165/v1

License: This work is licensed under a Creative Commons Attribution 4.0 International License.
Read Full License

Additional Declarations: There is **NO** Competing Interest.

Abstract

Direct air capture requires sorbents that bind CO_2 selectively yet release it with low energy. Bis-iminoguanidines capture CO_2 by crystallizing as hydrated carbonate salts, but the molecular events linking water loss, proton transfer, and CO_2 release remain unresolved. Here we combine variable-temperature single-crystal neutron and X-ray diffraction with *ab initio* molecular dynamics to determine how two crystalline carbonate phases follow different regeneration pathways. We show that lattice water acts as a molecular gate for carbonate protonation. In a metastable phase, water is isolated from carbonate, creating a softer hydrogen-bond network that promotes surface proton transfer and a transient carbonic-acid configuration. In the stable phase, water hydrogen-bonds directly to carbonate, stabilizing the lattice and suppressing proton transfer until water rearrangement and partial desorption disrupt the hydration environment. Controlling hydration topology together with targeted hydrogen-bond flexibility offers a route to direct-air-capture sorbents that retain selective CO_2 binding while lowering regeneration energy.

Main

Direct air capture (DAC) offers a scalable route to carbon removal, but sorbents must bind CO_2 at atmospheric partial pressure and release it with minimal heat input.[1–3,] Bis-iminoguanidines (BIGs) meet the capture requirement through reactive crystallization of hydrated carbonate salts from air.[4–6, 7,8] Heating to 80–120°C releases CO_2 and H_2O and regenerates the neutral BIG; however, strongly bound lattice water can dominate the energy penalty.[7,9] The crystal hydrogen-bond network is therefore part of the reaction coordinate rather than a passive structural scaffold.

Methyl-glyoxal-bis(iminoguanidinium) (MGBIG) carbonate forms two products with contrasting stability. The metastable P1 phase appears early during crystallization, whereas the denser P3 phase dominates at longer times.[7] X-ray structures and charge-density analysis at 100 K showed that these phases differ in packing, electron-density topology and hydrogen-bond cooperativity.[10] Such static structures cannot establish how proton transfer, water reorientation and dehydration evolve near regeneration conditions, or why nominally equivalent proton donors respond differently in the two lattices.

Here we combine variable-temperature single-crystal neutron diffraction (SCND), single-crystal X-ray diffraction (SCXD) coupled with Hirshfeld atom refinement (HAR), and *ab initio* molecular dynamics (AIMD). SCND directly locates hydrogen atoms and determines their anisotropic displacement parameters,[11] while HAR provides an independent X-ray description of the same hydrogen-bond network.[11] The experiments track hydrogen-bond geometries, atomic motion and site occupancies from 100 K to near regeneration temperatures; the simulations resolve time-dependent bulk and interfacial pathways. We find that water isolated from carbonate in P1 permits site-selective proton transfer and transient double protonation at the interface. In P3, direct water–carbonate hydrogen bonds suppress

proton transfer until water coordination weakens. These results identify hydration topology, rather than hydration level alone, as a control variable for regeneration-relevant solid-state reactivity.

By correlating site-specific hydrogen-bond geometry, displacement parameters and occupancies with AIMD trajectories, we test why N6–H6 transfer is favored in P1 although the same nominal donor group is present in P3, and how water motion enables the first steps toward CO_2 and H_2O release. The comparison reframes sorbent design around selective proton-transfer pathways and releasable hydration motifs rather than indiscriminate lattice destabilization.

Results

Crystal structures and thermal expansion of P1 and P3

MGBIG carbonate hydrates corresponding to P1 and P3 were prepared by established procedures.[7] Variable-temperature X-ray data were collected at 100, 300, 310 and 320 K for P1 and at 100, 300, 320 and 340 K for P3. Neutron Laue data were collected on TOPAZ at corresponding temperatures, with the highest-temperature P3 measurement at 343 K.[12,13] For direct comparison of bond distances, neutron refinements used unit-cell parameters from the corresponding X-ray measurements. The neutron and HAR structures are shown in Fig. 1.

Both structures are monoclinic, with space groups $P2/n$ for $P1$ and $P2_1/c$ for P3, and neither shows a crystallographic phase transition over the measured range. The X-ray unit-cell volume increases by 4.45% for P1 and 4.32% for P3, with the largest expansion along a in both phases. Neutron data reproduce the same anisotropic trends, although the measured volume increases are smaller (2.48% and 3.18%, respectively). Full lattice parameters and linear fits are provided in Figs. S1 and S2 and Tables S1 and S4–S11.

Neutron and HAR heavy-atom geometries agree closely throughout the temperature series (Figs. 1 and S3). Carbonate C–O, glyoxal C–C and guanidinium C–N and N–N distances show only small changes, confirming that the covalent frameworks remain intact. The detailed intramolecular distances and angles are provided in Tables S12–S15, while Tables S16 and S17 collect the neutron-derived hydrogen-bond geometries used below.

For P1, the O1–C6 carbonate bond and representative C–C, N–N and C–N distances remain closely matched between neutron and HAR models from 100 to 320 K. The C3–C2 distance is effectively temperature independent, and the N6–N5, N3–N4, N8–C5, N2–C1 and N1–C1 distances show only minor variations within their experimental uncertainties. Heating therefore changes the intermolecular hydrogen-bond network without measurably altering the molecular connectivity of P1.

P3 shows similarly close agreement at low and intermediate temperatures. At 340–343 K, small neutron/HAR differences emerge for selected carbonate bonds: O2–C6 is 1.297/1.290 Å, O3–C6 is 1.289/1.280 Å and O1–C6 is 1.293/1.291 Å. Selected glyoxal C–C and guanidinium C–N distances also

diverge slightly, whereas most N–N and C–N distances remain comparable. The magnitude and site selectivity of these differences are consistent with increasing thermal motion and dynamic disorder, not a change in bonding.

HAR X–H distances are generally shorter than neutron values, with an average difference of about 0.02 Å across both phases. In P1, the mean differences are approximately 0.027 Å for N–H bonds and 0.039 Å for water O–H bonds; the corresponding P3 differences are smaller and less systematic. Despite these offsets, HAR reproduces the ordering of the principal hydrogen bonds and their overall temperature dependence. We therefore use neutron distances as the direct metric of proton position and HAR as an independent measure of the same structural trends.

Ab initio molecular dynamics of hydrogen-bonded proton motion in P1 and P3

AIMD simulations were performed for bulk P1 and P3 at 320 and 400 K and for their lowest-free-energy solid–vacuum interfaces, P1(100) and P3(001), at 453 K (Methods). The higher temperatures enhance sampling of rare proton-transfer and water-rearrangement events and are used to identify accessible pathways rather than equilibrium rates. The 2 × 2 × 2 bulk supercells and relaxed slab models contain multiple equivalent hydrogen-bond environments, so every proton-involving atomic pair was analyzed rather than relying on one representative trajectory. Average distances are compared with neutron values in Tables S2 and S3, and site-resolved distributions are given in Tables S18–S23.

P1 displays the more accessible proton-transfer landscape. Transfer of H6 from guanidinium to the nearest carbonate oxygen occurs for all equivalent sites in the bulk at 400 K and is also sampled in the 453 K interface trajectory (Fig. 3a,b). No comparable H8B transfer occurs in either environment (Fig. S4a), demonstrating that the response is controlled by the local pathway rather than the formal donor type. At the interface, transfer coordinates for the two H6 protons associated with one carbonate are strongly anticorrelated (Pearson coefficient − 0.841; Fig. 3c), but occasional sequential transfer still yields a transient doubly protonated carbonate configuration consistent with carbonic acid (Fig. 3d). Decomposition into H_2O and CO_2 is not observed within the simulated time window, so this configuration is assigned as a plausible interfacial precursor rather than a complete simulated release event.

P3 resists proton transfer in the hydrated bulk: no migration from H6, H8B or other analyzed sites is observed at 320 or 400 K (Figs. 4a and S5). At the 453 K interface, H6 transfer becomes accessible in all equivalent N6–H6···O1 environments but remains less extensive than in P1 (Fig. 4c); N3–H3···O2 transfer is rare and localized. The H3 and H6 transfer coordinates are weakly anticorrelated (− 0.223), and no carbonic-acid configuration is observed (Fig. S8a). H6 transfer correlates positively with increasing distances between carbonate oxygens and coordinating water protons (+ 0.381; Figs. 4e and S8b), whereas the infrequent H3 events show no resolvable correlation. The trajectory is consistent with loss of direct water coordination preceding access to the principal H6 pathway in P3 and supports the phase-dependent pathways summarized in Fig. 5.

Water remains localized at its crystallographic sites in both bulk phases, although rotational motion increases at 400 K. In P1, the water molecule repeatedly reorients in place, alternating which proton hydrogen-bonds to neighboring nitrogen acceptors without translational diffusion (Figs. S4b,c). P3 bulk water similarly exhibits site-confined reorientation (Fig. 4b). These motions broaden water-related distance distributions but do not themselves constitute water-to-carbonate proton transfer.

The interfaces separate the two water responses more clearly. Surface water in P3 becomes weakly coordinated, moves laterally between neighboring carbonate anions and eventually desorbs (Figs. 4d,f,g and S10). P1 also exhibits interfacial water motion, but its translational mobility is lower (Fig. S9). Thus, P1 accesses carbonate protonation within a soft hydrogen-bond network, whereas P3 first requires disruption of direct water–carbonate coordination. At 320 K, the AIMD-averaged H···acceptor distances reproduce the principal ordering measured by neutron diffraction in both phases. Raising the bulk temperature to 400 K then broadens the P1 H6···O1 distribution and increases proton-transferred configurations, while the corresponding P3 distributions change little. This agreement links the trajectory-level events to the experimentally resolved hydrogen-bond environments.

Temperature-dependent hydrogen bonds and proton migration in P1

P1 shows the larger temperature-induced response of its hydrogen-bond network. From 100 to 320 K, selected guanidinium–carbonate and guanidinium–water donor–acceptor contacts lengthen modestly (Fig. 1a). The H6···O1 contact remains among the shortest H···O distances, while N6–H6 changes only slightly. Together with elongation of N6···O1 and increasing H6 displacement amplitude, this geometry indicates enhanced mobility along N6–H6···O1, not a monotonic static displacement. AIMD supports this assignment: H6···O1 fluctuations increase from 320 to 400 K and proton-transferred configurations become more frequent (Table S2 and Fig. 3a).

The short H8B···O2 contact varies non-monotonically with temperature and therefore does not establish progressive H8B migration. AIMD likewise shows no transfer along this pathway (Fig. S4a). Water-related O–H distances are also non-monotonic, and neither neutron nor HAR data establish water-to-carbonate proton transfer. Instead, AIMD shows in-place rotation at 400 K, with hydrogen-bond switching between the two water protons and neighboring nitrogen acceptors but no translational water diffusion (Figs. S4b,c).

Hydrogen ADPs quantify this thermal softening. Neutron B-factors for H6, H8B and the water hydrogen H3B increase from 1.69, 2.02 and 2.31 $Å^2$ at 100 K to 4.11, 4.42 and 4.42 $Å^2$ at 320 K, respectively (Fig. 2a). HAR gives the same qualitative trend (Figs. 2b and S7). The combined bond geometries and ADPs identify a dynamically softer network, with the clearest evidence for proton sharing localized to N6–H6···O1.

The anisotropy of the hydrogen ellipsoids is also informative. H6 elongates primarily along the N6–H6···O1 direction, linking the increased ADP to motion along the proton-transfer coordinate rather than to isotropic disorder. H8B also becomes more mobile, but its H8B···O2 distance does not shorten

systematically. The same increase in amplitude can therefore have different chemical consequences at neighboring sites.

HAR refinements support a thermally softened P1 hydrogen-bonding region, although their absolute X–H distances are shorter and individual temperature trends do not match the neutron series at every site. The mechanistic assignment therefore rests on the combined neutron geometry, directional ADPs and AIMD trajectories, not on a single X–H distance.

Chemically, the contrast between H6 and H8B shows that proton transfer is governed by the surrounding hydrogen-bond network within the delocalized guanidinium framework. A short H···O contact alone is insufficient; the lattice must also provide a sufficiently flexible collective coordinate for transfer.

Structural stability and hydrogen-bond evolution in P3

P3 responds more locally to heating. Its guanidinium–carbonate framework changes little from 100 to 343 K, and the principal donor–acceptor contacts remain comparatively rigid (Fig. 1b). Unlike P1, P3 contains direct water–carbonate hydrogen bonds. Neutron data show only modest changes in O3···O4 and O5···O1 contacts and nearly temperature-independent O–H distances. HAR shows increasing N···O distances and elongation of N8–H8B, while N6–H6 remains nearly unchanged. The dominant experimental response is a marked decrease in the refined occupancy of water hydrogen H7 (Fig. 2e), indicating increasing disorder and possible incipient dehydration at this site.

The P3 surface simulations connect this local disorder to proton transfer. At 453 K, water–carbonate coordination weakens, surface water becomes mobile and desorption occurs before N6–H6···O1 transfer becomes accessible (Fig. 4c–g). In the bulk, by contrast, the AIMD-averaged O1···H6 distance remains 1.754–1.755 Å from 320 to 400 K with an unchanged spread of approximately 0.170 Å, consistent with the limited structural response measured by diffraction (Table S3). P3 therefore preserves its guanidinium–carbonate framework until disruption of the directly coordinating water sublattice creates a proton-transfer pathway.

Atom-specific displacement parameters support this localization. Carbonate-directed H6 and H8B show gradual B-factor increases, whereas the largest changes occur in the hydrated region. H7 retains a large B-factor throughout the neutron series and increases strongly in HAR at elevated temperature, consistent with its decreasing occupancy. The diffraction response therefore is consistent with the water sublattice, rather than the guanidinium–carbonate framework, being the first region destabilized on heating. Because H7 belongs to a water molecule that participates in the direct hydration network around carbonate, its reduced occupancy perturbs the local hydrogen-bonding environment around carbonate. This site-specific disorder is therefore chemically distinct from a uniform increase in lattice vibration.

This behavior differs from P1 in both location and sequence. P1 distributes thermal motion across a soft network and permits H6 transfer without prior water loss. P3 confines its initial disorder to directly

coordinating water sites; only after their hydrogen bonds weaken does carbonate protonation become accessible at the interface.

Debye–Waller factors and dynamic disorder

Average Debye–Waller factors reinforce the site-specific analysis (Fig. 2 and Fig. S7). Both neutron and X-ray data show a stronger overall temperature response for P1, consistent with increased motion across the molecular ions and water. P3 also displays the expected thermal increase, but its excess response is concentrated in the hydrated region rather than distributed uniformly through the framework. The distinction is therefore not whether either lattice moves on heating, but where the additional disorder is accommodated. P1 is dynamically softer across the guanidinium–carbonate–water network; P3 retains a comparatively rigid guanidinium–carbonate framework and channels thermal disorder into the water sublattice. This pattern is consistent across the average B-factors, atom-specific hydrogen ADPs and refined occupancies, providing three independent crystallographic measures of the same phase-dependent response.

Discussion

The combined diffraction and AIMD data establish hydration topology as the principal distinction between the thermally activated responses of P1 and P3 (Table 1). In P1, water is separated from carbonate and participates in a cooperative but comparatively soft hydrogen-bond network. Heating increases hydrogen motion throughout this network, while H6 selectively samples proton-shared and transferred configurations. At the interface, sequential H6 transfer can generate a transient carbonic-acid configuration. In P3, direct water–carbonate hydrogen bonds stabilize the carbonate environment; proton transfer remains suppressed until water coordination is disrupted.

Table 1
Structural and dynamical features governing regeneration in the two MGBIG carbonate phases

Feature	Metastable phase	Stable phase
Water–carbonate topology	Water isolated from carbonate	Water directly hydrogen-bonded to carbonate
Guanidinium–carbonate network	Softer and less and constrained	More rigid and strongly stabilized
Bulk H6 transfer	Observed in AIMD at elevated temperature	Not observed in hydrated bulk
Water response	Predominantly localized reorientation	Rearrangement and partial desorption at the interface
Interfacial protonation	Extensive H6 transfer; transient double protonation	H6 transfer follows loss of water coordination
Carbonic-acid configuration	Observed transiently	Not observed
Regeneration implication	Proton transfer is readily accessible	Water loss acts as the gate to proton transfer

The two methods resolve complementary aspects of this mechanism. Diffraction provides temperature-dependent average structures, occupancies and ADPs, but does not by itself identify individual proton-transfer events. AIMD resolves those events and connects them to water coordination. The elevated-temperature simulations accelerate sampling and define plausible atomistic pathways, not equilibrium populations, kinetic barriers or regeneration rates. Agreement between the experimental displacement trends and the simulated site-selective motion supports the mechanistic assignment without treating the trajectories as a direct kinetic model.

This distinction also separates static hydrogen-bond polarization from thermally accessible proton motion. Our earlier charge-density study found strong O···H6 polarization, particularly in P3, yet the present data show that polarization alone does not predict transfer. A strongly polarized bond can remain confined by a rigid lattice, whereas a less constrained local environment can sample proton-shared configurations. The relevant control variable is therefore the combination of local bond geometry and collective lattice flexibility.

These pathways clarify, but do not directly measure, the regeneration-energy landscape. P1 can reorganize through selected proton motion and water reorientation before extensive dehydration. P3 instead localizes its initial response in specific hydration sites, making water disorder and loss the gate to carbonate protonation. This mechanistic contrast explains why crystals formed by the same molecular sorbent can follow different regeneration-relevant pathways. It does not imply that the metastable phase must have the lower overall regeneration enthalpy, because lattice cohesion, dehydration and subsequent chemical steps all contribute. Rather, the data identify which microscopic

coordinates become accessible first and therefore which structural features can be modified without assuming a single bulk-energy descriptor.

Design implications and conclusion

Three design principles follow from this phase-resolved mechanism.

1. Phase control determines the accessible regeneration pathway.

Packing and hydrogen-bond topology should be treated as primary design parameters because metastable and stable carbonate phases distribute proton and water motion differently. Controlling nucleation and phase selection may therefore alter regeneration behavior without changing the molecular sorbent.

2. Hydrogen-bond flexibility should be localized rather than maximized.

The selective H6 response in P1 shows that a thermally accessible protonation pathway can coexist with a short, non-transferring H8B···O2 bond. Substitution should target one dominant pathway while preserving stiffness elsewhere in the lattice, limiting unproductive relaxation and structural instability.

3. Strongly connected water sites are rational targets for weakening.

The decrease in H7 occupancy and interfacial water mobility in P3 identify specific hydration motifs that may add to the water-removal penalty. Steric or hydrophobic modifications that reduce their connectivity could lower the cost of dehydration without eliminating selective carbonate binding. Such modifications should be evaluated site by site rather than through total water content alone.

In summary, variable-temperature neutron and X-ray diffraction combined with AIMD connect hydration topology to proton motion and water loss in crystalline MGBIG carbonates. Lattice water acts as a molecular gate: its placement determines whether carbonate protonation is accessible within a soft network or requires prior dehydration. This principle provides a chemically specific basis for engineering reactive-crystallization sorbents that retain selective CO_2 binding while avoiding unnecessary lattice stabilization.

Methods

Crystal growth

MGBIG carbonate hydrates corresponding to phases P1 and P3 were synthesized and crystallized from aqueous solution following published procedures.[7] Single crystals suitable for neutron and X-ray diffraction were selected under a microscope and mounted on MiTeGen loops with superglue or Krytox grease as appropriate.

Single-crystal X-ray diffraction and Hirshfeld atom refinement

X-ray diffraction data were collected at 100, 300, 310 and 320 K for P1 and at 100, 300, 320 and 340 K for P3 using a Rigaku XtaLAB Mini II diffractometer with Mo Kα radiation (λ = 0.71073 Å) and a hybrid pixel array detector. Standard data-reduction procedures were applied. Structures were solved by direct methods and refined by Hirshfeld atom refinement (HAR) to obtain accurate hydrogen positions and anisotropic displacement parameters. Molecular wavefunctions were computed using the ORCA package[14,15] employing density functional theory with the PBE exchange-correlation functional[16,17] and the cc-pVTZ basis set. The HAR was performed using the NoSpherA2[18,19] implemented in the Olex2 interface.[20] Heavy atoms were refined anisotropically; all hydrogen atoms located from difference Fourier maps were refined with anisotropic displacement parameters.

Single-crystal neutron diffraction

Time-of-flight Laue neutron diffraction experiments were carried out on the TOPAZ beamline at the Spallation Neutron Source (SNS), Oak Ridge National Laboratory.[13] Crystals were mounted in sealed capillaries, and data were collected at the same nominal temperatures as the X-ray study. Data normalization, including spectrum correction, Lorentz factors and detector efficiency, followed established procedures.[12,13] A wavelength-dependent absorption correction using $\mu = 1.6043 + 1.0766\lambda$ cm^{-1}, where λ is in Å, was applied. Reflections were written in SHELX HKLF2 format with individual wavelengths stored for each reflection and were not merged. Refinements were performed in SHELXL via Olex2.[20] Hydrogen atoms were located from Fourier maps, and their coordinates and anisotropic displacement parameters were freely refined.

Computational details

We used the experimental cell parameters of P1 and P3 at 320 K and extrapolated cell parameters at 400 K and 453 K based on the X-ray-measured temperature dependence of the lattice constants. The internal coordinates were then optimized at fixed cell parameters. 2 × 2 × 2 supercells of both phases were then created and used for *ab initio* molecular dynamics (AIMD) simulations with the CP2K package.[21] To investigate water mobility and proton transfer at the solid–vacuum interface, slab models exposing the (100) crystallographic surface of P1 and the (001) crystallographic surface of P3 were constructed and separated by a 16 Å vacuum region. These slabs were generated by cleaving the optimized bulk structures along planes defined by the guanidinium moieties, thereby producing the lowest-free-energy surface terminations, and were subsequently structurally relaxed prior to the AIMD simulations. Bulk AIMD simulations were performed at 320 K and 400 K, while the crystal–vacuum interface simulations were performed at 453 K. Simulations were performed using the PBE[16,17] exchange-correlation (XC) functional in conjunction with Grimme's D3(0) dispersion correction.[22] The electronic structure was described with the MOLOPT-DZVP basis sets[23] together with the Goedecker-Teter-Hutter (GTH) pseudopotentials[24] using a plane-wave cutoff of 400 Ry for the electron density. All simulations were performed in the canonical (NVT) ensemble using the Nosé-Hoover thermostat[25,26] and a 1 fs time step, and production runs were carried out for approximately 100 ps. Atomic trajectories

were explicitly exported throughout the simulations to enable post-processing and time-resolved structural analysis of proton dynamics, water reorientation, and bond-length fluctuations along the AIMD trajectories. Trajectory analysis and bond length calculations over the 20–100 ps interval were performed using in-house analysis scripts.

Declarations

This manuscript has been authored by UT-Battelle, LLC, under Contract DE-AC05-00OR22725 with the U.S. Department of Energy (DOE). The U.S. government retains and the publisher, by accepting the article for publication, acknowledges that the U.S. government retains a nonexclusive, paid-up, irrevocable, worldwide license to publish or reproduce the published form of this manuscript, or allow others to do so, for U.S. government purposes. DOE will provide public access to these results of federally sponsored research in accordance with the DOE Public Access Plan (https://www.energy.gov/doe-public-access-plan).

Data availability

The data supporting the findings of this study are available within the paper and its Supplementary Information. The crystallographic data for the P1 and P3 phases have been deposited with the Cambridge Crystallographic Data Centre under deposition numbers CCDC under deposition numbers 2591699–2591714. Copies of these data can be obtained free of charge from the CCDC at https://www.ccdc.cam.ac.uk/structures/. The data supporting the other findings of this study are provided within the Article and its Supplementary Information. The CP2K input files, starting structures, AIMD trajectories and underlying numerical data are available from the corresponding author upon request..

Code availability

All in-house scripts developed in this work for tracking and analyzing distances, as well as generating histograms for the hydrogen-bonding pairs of interest, are available through an open-access repository. The code includes sufficient documentation and usage instructions to enable reproducibility of the analyses and figures presented in this study.

Acknowledgements

This research used resources at the Spallation Neutron Source, a U.S. Department of Energy (DOE) Office of Science User Facility operated by Oak Ridge National Laboratory. Beam time was allocated on TOPAZ under proposals IPTS-31313.1 and IPTS-33368.1. The author contributions from T.J.P.S., D.R., J.D.E., R.C., and V.S.B. were supported by the U.S. Department of Energy, Office of Science, Basic Energy Sciences, Chemical Sciences, Geosciences, and Biosciences Division. The computational part of this research employed resources of the Oak Ridge Leadership Computing Facility at ORNL, which is supported by the Advanced Scientific Computing Research programs in the Office of Science of the U.S.

Department of Energy under Contract No. DE-AC05-00OR22725. This research also used resources of the National Energy Research Scientific Computing Center (NERSC), a Department of Energy User Facility using NERSC award BES-ERCAP-0035918. S.P. is grateful for the financial support from the Spanish Ministerio de Ciencia e Innovación and Consejo Superior de Investigaciones Científicas under Grant Nos. 2010 6O E 013 and 2021 60 E 030, and the Severo Ochoa Centres of Excellence program through Grant CEX2024-001445-S.

Note: This manuscript has been authored by UT-Battelle, LLC, under contract DE-AC05-00OR22725 with the US Department of Energy (DOE). The US government retains and the publisher, by accepting the article for publication, acknowledges that the US government retains a nonexclusive, paid-up, irrevocable, worldwide license to publish or reproduce the published form of this manuscript, or allow others to do so, for US government purposes. DOE will provide public access to these results of federally sponsored research in accordance with the DOE Public Access Plan (https://www.energy.gov/doe-public-access-plan).

Author contributions

S.P.: Conceptualization, Methodology, Data curation, Validation, Investigation, Visualization, Formal analysis, Writing – original draft, Writing – review & editing; T.J.P.S.: Methodology, Data curation, Validation, Investigation, Formal analysis, Visualization, Writing – review & editing; D.R.: Methodology, Data curation, Validation, Formal analysis, Writing – original draft; J.D.E.: Data curation, Validation, Resources, Writing – original draft; R.C.: Conceptualization, Project administration, Funding acquisition, Writing – original draft, Writing – review & editing; V.S.B.: Conceptualization, Methodology, Data curation, Validation, Writing – original draft, Writing – review & editing; X.W.: Conceptualization, Project administration, Funding acquisition, Methodology, Data curation, Formal analysis, Writing – original draft, Writing – review & editing.

Competing interests

The authors declare no competing interests.

References

1. Sanz-Perez, E. S., Murdock, C. R., Didas, S. A. & Jones, C. W. Direct Capture of CO_2 from Ambient Air. *Chem Rev* **116**, 11840–11876 (2016). https://doi.org/10.1021/acs.chemrev.6b00173
2. Erans, M. *et al.* Direct air capture: process technology, techno-economic and socio-political challenges. *Energy & Environmental Science* **15**, 1360–1405 (2022). https://doi.org/10.1039/d1ee03523a
3. Custelcean, R. Direct Air Capture of CO_2 Using Solvents. *Annu Rev Chem Biomol Eng* **13**, 217–234 (2022). https://doi.org/10.1146/annurev-chembioeng-092120-023936

4. Seipp, C. A., Williams, N. J., Kidder, M. K. & Custelcean, R. CO_2 Capture from Ambient Air by Crystallization with a Guanidine Sorbent. *Angew Chem Int Ed Engl* **56**, 1042–1045 (2017). https://doi.org/10.1002/anie.201610916
5. Stamberga, D., Einkauf, J. D., Liu, M. & Custelcean, R. Direct Air Capture of CO_2 via Reactive Crystallization. *Crystal Growth & Design* **24**, 4556–4562 (2024). https://doi.org/10.1021/acs.cgd.4c00201
6. Custelcean, R. Direct air capture with bis-iminoguanidines: From discovery to commercialization. *Chem* **7**, 2848–2852 (2021). https://doi.org/10.1016/j.chempr.2021.10.001
7. Custelcean, R. *et al.* Dialing in Direct Air Capture of CO_2 by Crystal Engineering of Bisiminoguanidines. *ChemSusChem* **13**, 6381–6390 (2020). https://doi.org/10.1002/cssc.202001114
8. Custelcean, R. Direct air capture of CO_2 via crystal engineering. *Chem Sci* **12**, 12518–12528 (2021). https://doi.org/10.1039/d1sc04097a
9. Kasturi, A. *et al.* Determination of the regeneration energy of direct air capture solvents/sorbents using calorimetric methods. *Separation and Purification Technology* **310** (2023). https://doi.org/10.1016/j.seppur.2023.123154
10. Pawledzio, S., Einkauf, J., Custelcean, R. & Wang, X. Intermolecular Interactions in Direct Air Capture Materials: Insights from Charge Density Analysis. *Journal of the American Chemical Society* **147**, 27299–27313 (2025). https://doi.org/10.1021/jacs.5c01946
11. Capelli, S. C., Burgi, H. B., Dittrich, B., Grabowsky, S. & Jayatilaka, D. Hirshfeld atom refinement. *IUCrJ* **1**, 361–379 (2014). https://doi.org/10.1107/S2052252514014845
12. Schultz, A. J. *et al.* Integration of neutron time-of-flight single-crystal Bragg peaks in reciprocal space. *Journal of Applied Crystallography* **47**, 915–921 (2014). https://doi.org/10.1107/s1600576714006372
13. Coates, L. *et al.* A suite-level review of the neutron single-crystal diffraction instruments at Oak Ridge National Laboratory. *Rev Sci Instrum* **89**, 092802 (2018). https://doi.org/10.1063/1.5030896
14. Neese, F. The ORCA program system. *WIREs Computational Molecular Science* **2**, 73–78 (2011). https://doi.org/10.1002/wcms.81
15. Neese, F. Software Update: The ORCA Program System—Version 6.0. *WIREs Computational Molecular Science* **15** (2025). https://doi.org/10.1002/wcms.70019
16. Perdew, J. P., Burke, K. & Ernzerhof, M. Generalized Gradient Approximation Made Simple. *Phys Rev Lett* **77**, 3865–3868 (1996). https://doi.org/10.1103/PhysRevLett.77.3865
17. Perdew, J. P., Burke, K. & Ernzerhof, M. Generalized Gradient Approximation Made Simple [Phys. Rev. Lett. 77, 3865 (1996)]. *Physical Review Letters* **78**, 1396–1396 (1997). https://doi.org/10.1103/PhysRevLett.78.1396
18. Kleemiss, F. *et al.* Accurate crystal structures and chemical properties from NoSpherA2. *Chem Sci* **12**, 1675–1692 (2020). https://doi.org/10.1039/d0sc05526c

19. Midgley, L. *et al.* Vanishing of the atomic form factor derivatives in non-spherical structural refinement - a key approximation scrutinized in the case of Hirshfeld atom refinement. *Acta Crystallogr A Found Adv* **77**, 519–533 (2021). https://doi.org/10.1107/S2053273321009086
20. Dolomanov, O. V., Bourhis, L. J., Gildea, R. J., Howard, J. A. K. & Puschmann, H. OLEX2: a complete structure solution, refinement and analysis program. *Journal of Applied Crystallography* **42**, 339–341 (2009). https://doi.org/10.1107/s0021889808042726
21. VandeVondele, J. *et al.* Quickstep: Fast and accurate density functional calculations using a mixed Gaussian and plane waves approach. *Computer Physics Communications* **167**, 103–128 (2005). https://doi.org/10.1016/j.cpc.2004.12.014
22. Grimme, S., Antony, J., Ehrlich, S. & Krieg, H. A consistent and accurate ab initio parametrization of density functional dispersion correction (DFT-D) for the 94 elements H-Pu. *J Chem Phys* **132**, 154104 (2010). https://doi.org/10.1063/1.3382344
23. VandeVondele, J. & Hutter, J. Gaussian basis sets for accurate calculations on molecular systems in gas and condensed phases. *J Chem Phys* **127**, 114105 (2007). https://doi.org/10.1063/1.2770708
24. Goedecker, S., Teter, M. & Hutter, J. Separable dual-space Gaussian pseudopotentials. *Phys Rev B Condens Matter* **54**, 1703–1710 (1996). https://doi.org/10.1103/physrevb.54.1703
25. Martyna, G. J., Klein, M. L. & Tuckerman, M. Nosé–Hoover chains: The canonical ensemble via continuous dynamics. *The Journal of Chemical Physics* **97**, 2635–2643 (1992). https://doi.org/10.1063/1.463940
26. Evans, D. J. & Holian, B. L. The Nose–Hoover thermostat. *The Journal of Chemical Physics* **83**, 4069–4074 (1985). https://doi.org/10.1063/1.449071

Figures

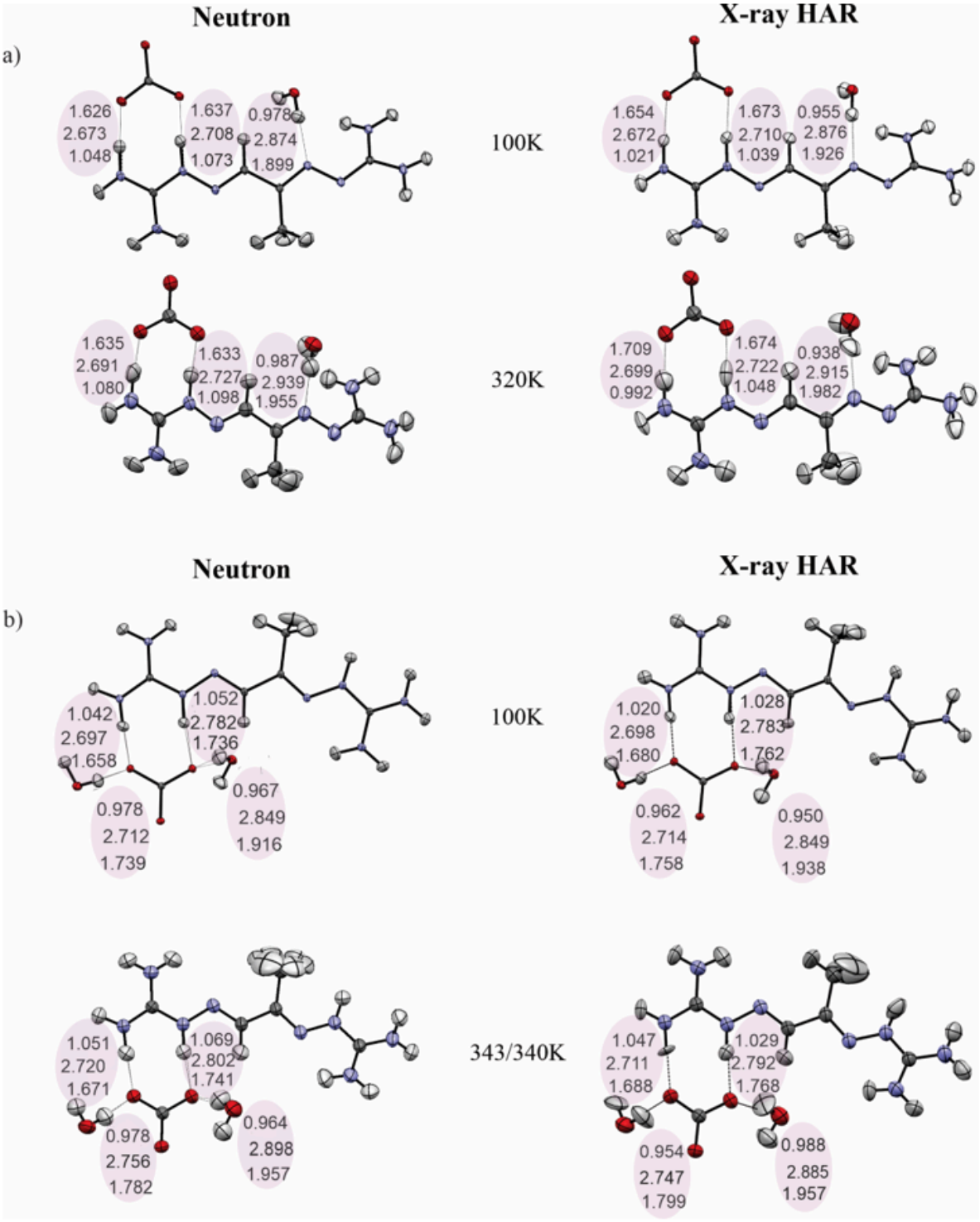


Figure 1

Contrasting hydration topologies of the two MGBIG carbonate phases. Variable-temperature neutron and X-ray structures of (a) P1 and (b) P3. Thermal ellipsoids are shown at the 50% probability level. Selected intermolecular hydrogen bond distances highlight the separation of lattice water from carbonate in P1 and direct water–carbonate hydrogen bonding in P3.

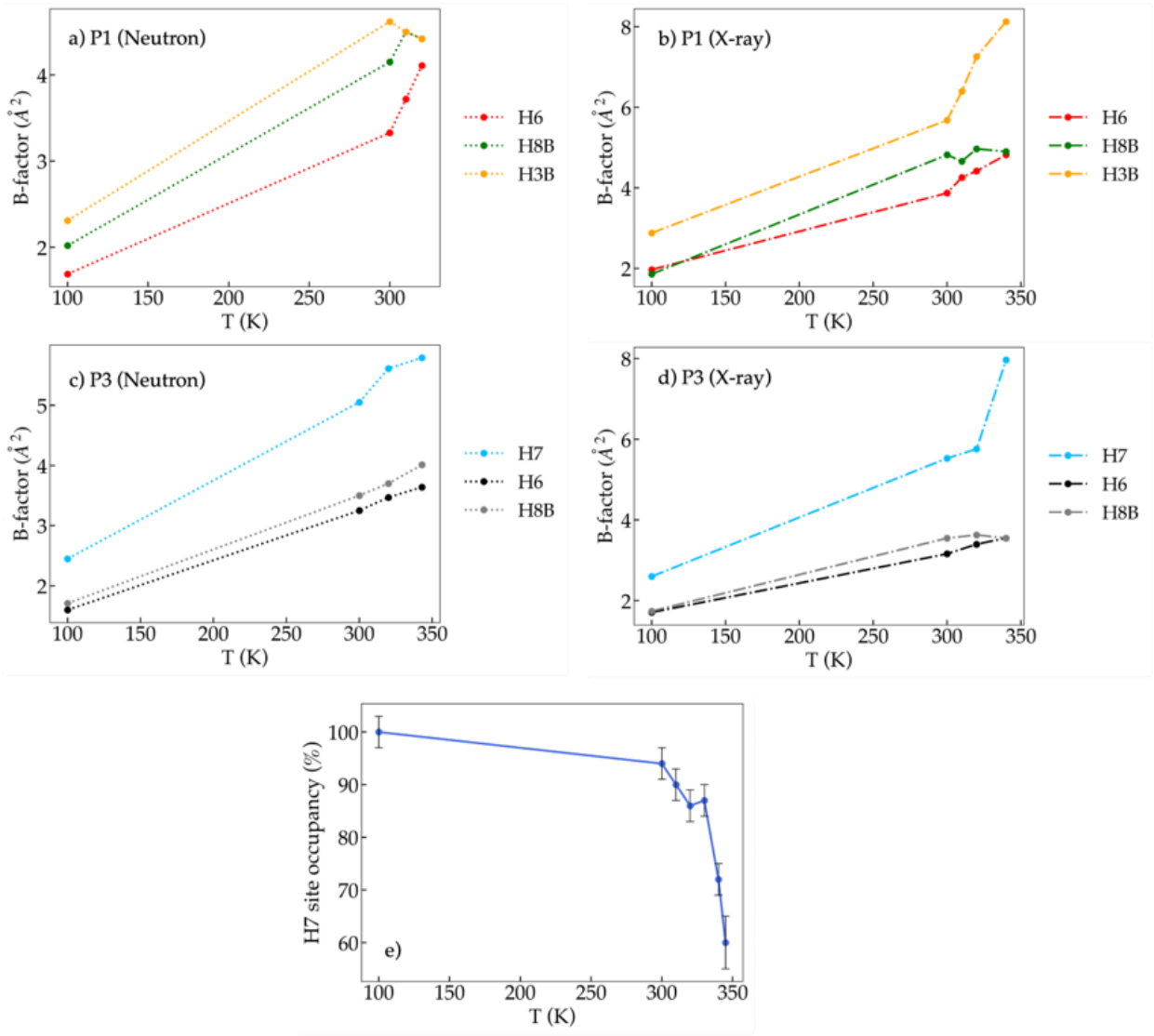


Figure 2

Selected hydrogen displacement parameters and H7 occupancy reveal phase-selective water disorder. Temperature dependence of selected Debye–Waller B-factors for P1 obtained from (a) neutron and (b) X-ray diffraction and for P3 obtained from (c) neutron and (d) X-ray diffraction. (e) Temperature dependence of the H7 site occupancy in the P3 phase.

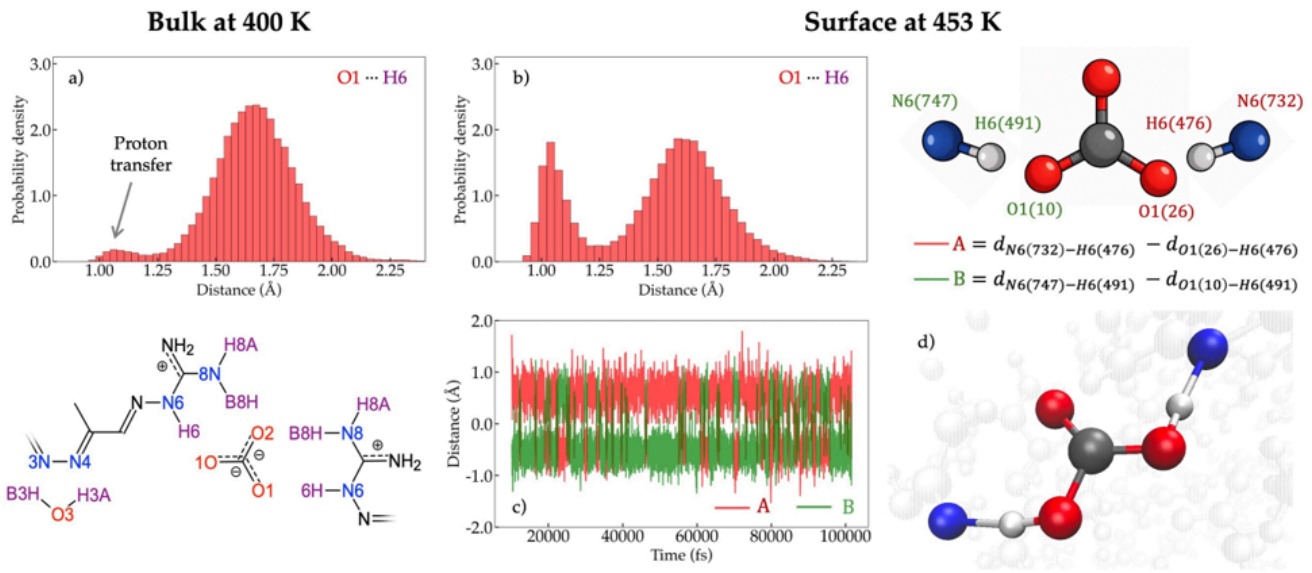


Figure 3

Interfacial proton transfer in P1 produces transient carbonic acid. (a) Probability distribution of the O1···H6 distance, showing occasional proton transfer events toward the carbonate oxygen at 400 K. (b) Probability distribution of the O1···H6 distance at the surface with a higher population of short O1···H6 configurations in the 453 K surface trajectory than in the 400 K bulk trajectory, demonstrating enhanced proton transfer character compared to the bulk. (c) Time-dependent proton transfer coordinates (A and B) for the two equivalent H6···O1 proton transfer pathways at the P1 solid-vacuum interface at 453 K. Positive values indicate proton transfer toward the acceptor oxygen, whereas negative values indicate proton localization at the donor site. The strong anticorrelation between the two time series indicates that simultaneous proton transfer at the equivalent sites is disfavored. (d) Snapshot of a doubly protonated carbonate configuration at the P1 (100) surface at 453 K.

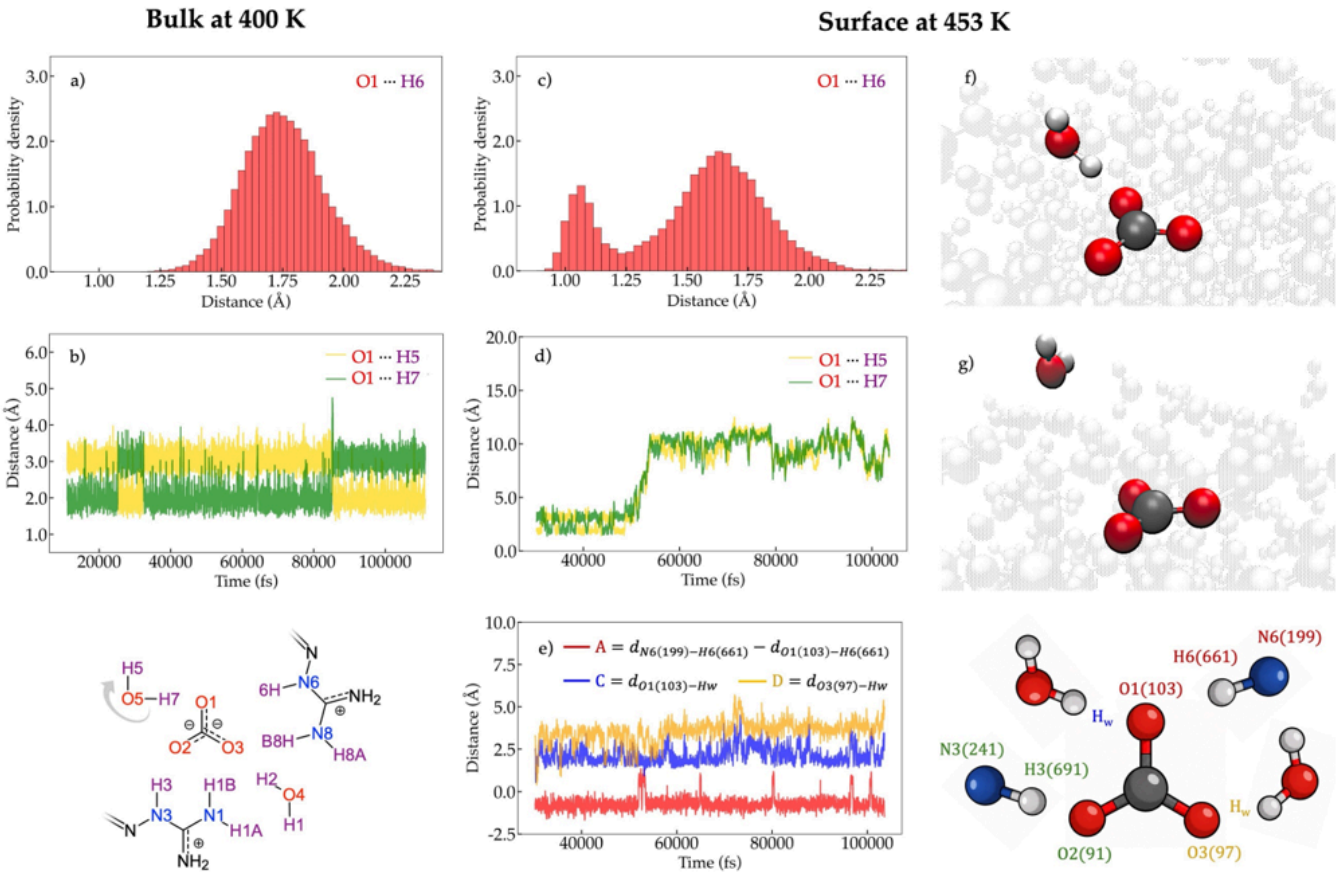


Figure 4

Loss of carbonate-bound water unlocks proton transfer in P3. (a) Probability distribution of the O1···H6 distances in the bulk P3 phase at 400 K, showing no proton transfer. (b) Time evolution of the O1···H5 and O1···H7 distances at 400 K, exhibiting fluctuations arising from water rotational motion. (c) Probability distribution of the O1···H6 distance at the surface, indicating enhanced proton transfer character compared to the bulk. (d) Time evolution of the O1–H5 and O1–H7 distances at the P3 (001) surface at 453 K, showing abrupt distance changes associated with water rearrangement and desorption. (e) Time evolution of the N6–H6···O1 proton-transfer coordinate A and carbonate–water distances C and D, showing positive correlation between carbonate dehydration and proton migration. (f) and (g) show representative snapshots before and after the water desorption event at the surface, respectively.

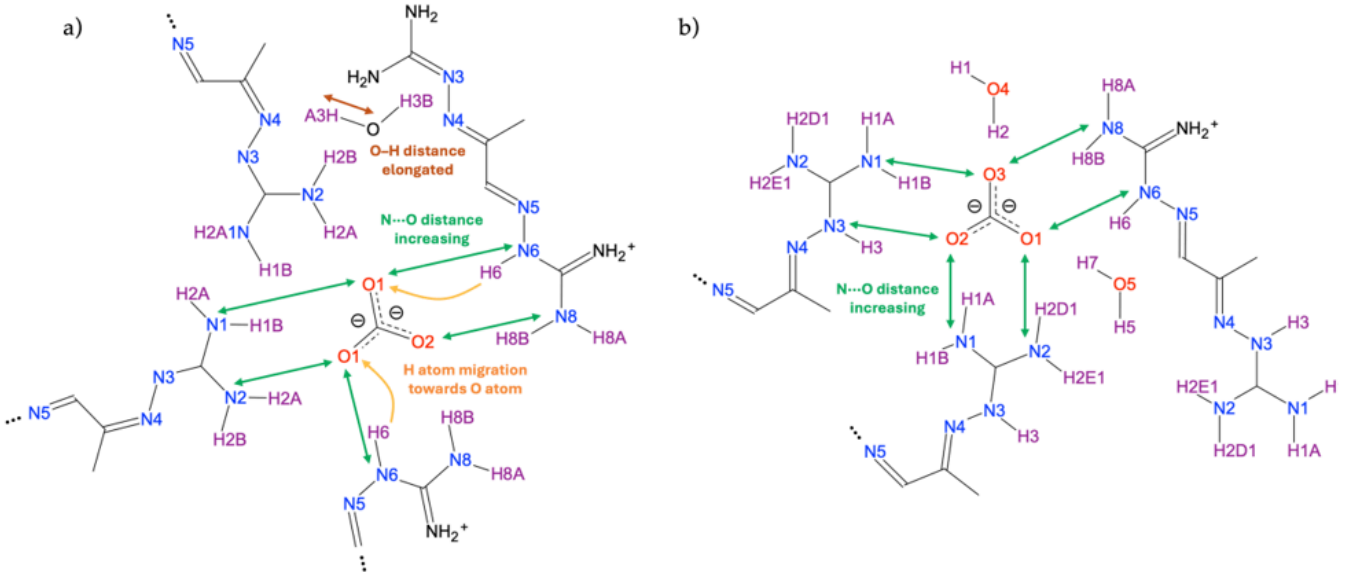


Figure 5

Water topology controls phase-dependent regeneration pathways. (a) In P1, lattice water is separated from carbonate, leaving a softer guanidinium–carbonate hydrogen-bond network that facilitates H6 proton transfer and transient carbonate double protonation at the surface. (b) In P3, direct water–carbonate hydrogen bonding stabilizes the carbonate environment and suppresses proton transfer until water rearrangement or partial desorption weakens carbonate hydration.

Supplementary Files

This is a list of supplementary files associated with this preprint. Click to download.

- P1P3CCDCStructures.zip
- BIGDACSupplementaryInformation.pdf